

To measure is to know

Evaluating indirect measurement techniques for observing the damage tolerance behaviour of spot welded thermoplastic composites

Smeets, Eva T.B.; Rans, Calvin D.; Castro, Saullo G.P.; Villegas, Irene F.

DOI

[10.1016/j.jajp.2023.100152](https://doi.org/10.1016/j.jajp.2023.100152)

Publication date

2023

Document Version

Final published version

Published in

Journal of Advanced Joining Processes

Citation (APA)

Smeets, E. T. B., Rans, C. D., Castro, S. G. P., & Villegas, I. F. (2023). To measure is to know: Evaluating indirect measurement techniques for observing the damage tolerance behaviour of spot welded thermoplastic composites. *Journal of Advanced Joining Processes*, 8, Article 100152. <https://doi.org/10.1016/j.jajp.2023.100152>

Important note

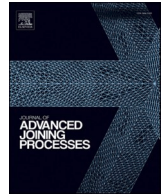
To cite this publication, please use the final published version (if applicable). Please check the document version above.

Copyright

Other than for strictly personal use, it is not permitted to download, forward or distribute the text or part of it, without the consent of the author(s) and/or copyright holder(s), unless the work is under an open content license such as Creative Commons.

Takedown policy

Please contact us and provide details if you believe this document breaches copyrights. We will remove access to the work immediately and investigate your claim.



To measure is to know: Evaluating indirect measurement techniques for observing the damage tolerance behaviour of spot welded thermoplastic composites

Eva T.B. Smeets^{*}, Calvin D. Rans, Saullo G.P. Castro, Irene F. Villegas

Aerospace Structures & Materials, Delft University of Technology, PO Box 5058, 2600 GB, Delft, the Netherlands

ARTICLE INFO

Keywords:

Ultrasonic spot welding
Thermoplastic composites
Damage growth
Digital image correlation (DIC)

ABSTRACT

In thermoplastic composite joints with a circular ultrasonic spot weld, the damage growth is located at the interface between the joined components. This means that any damage in these joints is invisible from the outside. This experimental study compares three different in-situ methods to measure the damage growth indirectly. The motivation lies in the potential benefits of using multi-spot welded joints for increased damage tolerance and the need to prove the damage arresting and damage progression behaviour for certification. The current study focused on measuring the damage in single-spot welded Single Lap Shear (SLS) joints during fatigue test with the global specimen compliance, the local out-of-plane displacement and the local strain on the surface. Digital Image Correlation (DIC) measurements were used to obtain the local quantities. The results showed that the local quantities are better suited to obtain detailed information on the damage state. The local surface strain showed more distinct features that facilitate the recognition of damage locations. The benefits and challenges of all methods are discussed as well as the difference in the level of detail, generalization and the prior knowledge necessary to obtain the damage state.

Introduction

Air travel is arguably the safest mode of long-distance transportation currently available to the general public. This can be attributed to the rigorous safety framework that is set up to ensure regulations are in place and to accidents being investigated such that they can be prevented in the future. The side effect of this framework is that the aviation sector is very conservative when it comes to safety. Existing and proven solutions are favoured over new ones, and any new technology is viewed through glasses that have been tinted by past experiences, in particular failures. This is aptly illustrated by looking at the adoption of a novel structural material in this sector: Carbon Fibre Reinforced Plastics (CFRPs). CFRPs are often promoted for their excellent specific strength and stiffness that can be tailored to the needs of any design application. Unlike metals, however, these advantages come with the possibility of anisotropic properties and a lack of ductility. To facilitate the application of CFRPs in aircraft primary structures, the so-called “black metal” approach was adopted where quasi-isotropic laminate configurations are applied in familiar structural configurations typically used in metals (SKF evolution, 2022). This arguably limited some of the potential

advantages offered by composites in terms of tailoring and fabrication possibilities but permitted the application of known structural concepts and design strategies to composites rather than a completely new structural concept. Indeed, new technologies must be considered in terms of the current safety framework for civil aviation and the existing pathways it provides and ignoring the concerns and safeguards put in place by past experience can be as much a barrier to progress as failing to consider that new technologies could deviate from these concerns and safeguards.

How does this relate to spot welding of thermoplastic composite materials? The ability to weld, rather than mechanically fasten or adhesively bond, is an attractive feature of thermoplastic composite materials. Mechanical fastening is an established joining technique in which the physical connection between the joined parts is immediately visible and inspectable; however, the holes needed to accommodate the fasteners weaken the composite material. Although adhesive bonding provides a structurally more efficient alternative to fastening, the risk of weak and/or kissing bonds within a bonded interface that is hidden from direct inspection (Jairaja and Naik, 2021) has limited the use of adhesive bonding in primary aircraft structures. This risk for weak and/or kissing

^{*} Corresponding author.

E-mail address: e.t.b.smeets@tudelft.nl (E.T.B. Smeets).

<https://doi.org/10.1016/j.jajp.2023.100152>

Received 21 December 2022; Received in revised form 16 May 2023; Accepted 17 July 2023

Available online 20 July 2023

2666-3309/© 2023 The Author(s). Published by Elsevier B.V. This is an open access article under the CC BY license (<http://creativecommons.org/licenses/by/4.0/>).

bonds is related to the complex processing conditions for the adhesive bonding process and the sensitivity of the chemistry within this process to variables such as surface contaminants along the distinct adhesive interfaces. Welding, being a fusion bonding process rather than an adhesive bonding process, overcomes many of these risks (Yousefpour et al., 2004). However, from a safety and certification standpoint, this does not necessarily mean that welded composite joints would be treated differently from adhesively bonded joints.

The current regulations for civil transport aircraft are described within 14 CFR part 25¹, with §25.571 covering fatigue and damage tolerance requirements. The regulations, however, often capture more of an intent rather than a means of compliance. For this reason, guidance documents, known as Advisory Circulars (AC), are published which detail the current experience-based accepted means of compliance with the regulations. Advisory Circular AC 20-107B (Federal Aviation Administration, 2009) describes an acceptable means of compliance² for composite structures. Concerning adhesively bonded joints, the AC states that for any bonded joint: *the failure of which would result in catastrophic loss of the aeroplane, the limit load capacity must be substantiated by one of the following methods*

- (i) *The maximum disbands of each bonded joint consistent with the capability to withstand the loads in (...) must be determined by analysis, tests, or both. Disbands of each bonded joint greater than this must be prevented by design features, or*
- (ii) *Proof testing must be conducted on each production article that will apply the critical limit design load to each critical bonded joint, or*
- (iii) *Repeatable and reliable non-destructive inspection techniques must be established that ensure the strength of each joint.*

Examining these three accepted means of compliance, it is clear that (i) is currently the most feasible and practical. Proof testing all production joints would be prohibitively expensive and logistically challenging for large primary aircraft structures and non-destructive testing techniques are adept at detecting physical damages at the interface, but not the reduced strength of a weak bond that does not have any damage. Here is where multi-spot welded thermoplastic composite joints offer a possibility. The discrete nature of the spot welded connections combined with the numerous possible patterns of spots in terms of spot size, spacing, and distribution provide an opportunity for tailoring the progressive failure behaviour and using this as the design feature for limiting damage growth according to (i). However, unlike the progressive pull-out failure mode in metallic spot welded joints (Zhou et al., 2006), fatigue damage in spot welded composite joints does not propagate into the joined parts where it can be directly observed and measured (Villegas and Bersee, 2010). Thus, indirect measurement techniques need to be used to detect and track damages in such joints. Classical Nondestructive Inspection (NDI) techniques such as ultrasonic C-scan and X-ray tomography are often used to inspect for damages, but they become less practical for prolonged and continuous monitoring during a fatigue test. Current in-situ monitoring techniques consist of visual inspection (ASTM Standard E647, 2016; Holzhüter et al., 2018), Acoustic Emission (AE) monitoring (Carboni and Bernasconi, 2021; Karimian and Modarres, 2021; Motta et al., 2020) and strain measurements using optic fibres or DIC (Lima et al., 2022; Rodi et al., 2009). However, each of these techniques comes with its challenges. For visual inspection, the damage should be visible from the side of the specimens. This is not achievable when using circular spot welds. AE monitoring

relies on damage initiation and growth generating sound waves. This means that it is feasible to determine the time at which an event occurs. The localization of damage using AE is slightly less straightforward and can only be done on a single line. Using strain measurements from optic fibres results in a determination of the damage location only with respect to the location of the fibre itself, determining the location on the specimen is not accurate. The current studies using DIC for damage localization determine the shape of the damage, but lack the quantification of the damage in the joint.

This creates a potential challenge for the certification of multi-spot welded composite joints. To convince the certification authorities of the damage arresting and damage progression behaviour of a multi-spot welded composite joint design, an indirect measurement technique that is more practical for prolonged and continuous fatigue testing is needed. In this study, several indirect measurement techniques - namely compliance measurements with an extensometer, surface displacement and surface strain measurements using Digital Image Correlation (DIC) - are evaluated in the context of characterizing damage progression in single-spot welded joints. In this study SLS specimens are used since they are straightforward to manufacture (Villegas and Rans, 2021). The purpose of this study is to identify the indirect measurement technique that is the most suited to measure the damage growth through the ultrasonic welds throughout the fatigue life. Ultimately, the goal is to increase the complexity of the analysed specimens and expand the technique to multi-spot joints where the adherends are joined with a configuration of multiple single-spot welds to represent a more realistic configuration. This study will also identify the possible benefits, challenges and limitations of each of the techniques with the analysis of the damage growth behaviour of multi-spot joints in mind.

Methodology

A series of experimental tests was carried out with SLS specimens. The specimens consisted of carbon fibre adherends with a Low Melt Polyaryletherketone (LMPAEEK) matrix that were joined with a single, circular ultrasonic spot weld at the centre of the overlap. The experiments were conducted under constant amplitude fatigue loading controlled by displacement. The goal of the experiments was to measure the damage growth, using displacement controlled fatigue loading ensured that the growth would be stable, thus making it easier to be captured.

A schematic representation of the specimens is shown in Fig. 1. The damage in the specimens occurs at the interface. As mentioned before, this poses a challenge since the interface cannot be observed directly. A set of Finite Element (FE) analyses was used to link the relevant features in the indirect measurements on the surface of the specimen to the damage location at the interface. The FE analyses provided insight into the phenomena occurring at the weld edges that would have to be found in the experimental data. This section first provides general information about the specimens. Then the set-up of the FE analyses is explained, followed by the details of the experimental tests and the procedure for processing the data from the indirect measurements.

Single lap shear (SLS) specimens and materials

The SLS specimen configuration was based on ASTM standard D5686 (ASTM Standard D5868-01, 2005) with an increased width and overlap

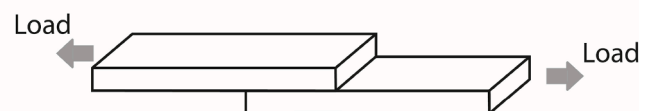


Fig. 1. Diagram of the SLS specimens.

¹ In the past this has been referred to as FAR part 25; however, due to potential confusion of FAR with *Federal Acquisition Regulations* instead of *Federal Aviation Regulations*, the FAA now prefers the full reference to Title 14 of the Code of Federal Regulations part 25, or 14 CFR part 25 for short.

² It is not the only possible means of compliance, but one that is currently accepted by the regulatory authorities.

length to accommodate the spot weld in the centre of the overlap. The nominal dimensions of the specimens are shown in Fig. 2. The adherends were made with 12 carbon fibre plies with an LMPAEK matrix, provided by Toray Advanced Composites in The Netherlands (Toray Advanced Composites, 2019). The lay-up was $[0/135/90/135/45/135]_s$. This lay-up was chosen due to its availability at the time, the lay-up was pre-made and provided externally, ensuring that the quality would be more consistent between the specimens than with a home-made laminate. The material properties for a single ply can be found in Table 1. The energy director used during the welding process was a discontinuous energy director of the same material as the matrix, LMPAEK.

Finite element (FE) analysis

The purpose of the FE analysis was to link the information of the different surface measurements to the knowledge about the damage at the interface. In the FE analysis the damage at the interface was artificially introduced at a known location. Different damage sizes were modelled to obtain a broader view of the features in the surface measurements that correspond to the interface damage. All the FE analyses were performed with Abaqus 2020 (Smith, 2020).

Damage sizes

The different damage sizes were modelled as welds of different shapes and sizes. Four different sizes of damage and three different growth directions were modelled, resulting in a total of ten different shapes. Fig. 3 shows the spot weld without damage and with three different damage sizes growing from both sides or from the right side. The spot welds with damage growing from the left side are a mirrored version of the right side. Table 2 lists the remaining weld area for every damage type.

Mesh specifications

The adherends were modelled with 8-noded continuum shell elements (SC8R) with a mesh size of 0.25 mm through the width of the specimens and 0.5 mm through the thickness. In the length direction, a 0.25 mm element length was used at the overlap and a 2 mm length outside of the overlap. The purpose of these analyses was to investigate the features on the surface that relate to the spot weld, the exact damage behaviour of the spot was not the main focus of interest. Therefore, the spot welds were modelled by applying a rigid tie between the nodes of both adherends that are part of the spot weld.

Boundary conditions

The boundary conditions for the FE analysis are shown in Fig. 4. The tab on the left side was fully clamped and a sliding support was applied to the tab on the right side. The loading was applied through a tensile displacement on the right tab.

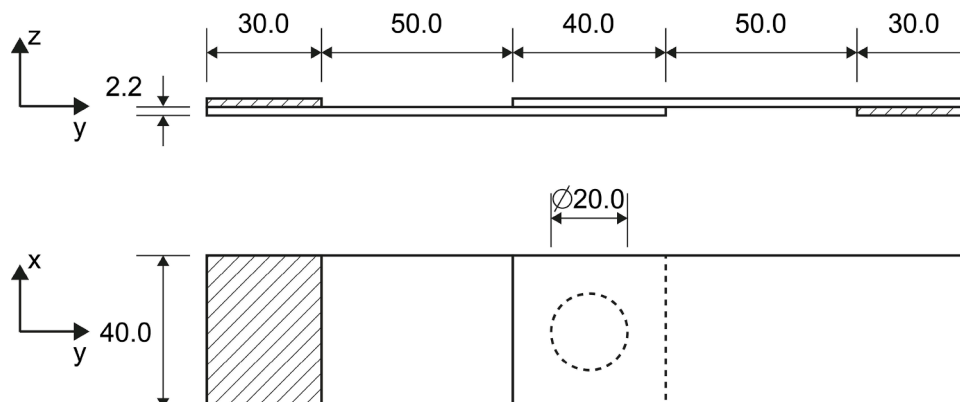


Fig. 2. Specimen dimensions.

Table 1
Standard modulus carbon UD tape material properties (Toray Advanced Composites, 2019).

Parameter [Unit]	Value
$\sigma_{max,xx}$ [MPa]	2410
$\sigma_{max,yy}$ [MPa]	86
$\sigma_{max,xy}$ [MPa]	152
E_{xx} [GPa]	135
E_{yy} [GPa]	10
E_{xy} [GPa]	4.3

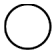






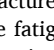
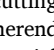
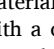


Fig. 3. Different damage types in FE analyses.

Loading details

For all the analyses, a dynamic implicit quasi-static load application with artificial damping was used to simulate the static loading conditions. To determine the applied displacement, the undamaged weld was loaded to 80% of the experimentally determined static failure load. The details can be found in Table 4. The undamaged specimen reached an opening displacement of 0.363 mm at this load. Since the fatigue experiments were conducted with a constant displacement, the same opening displacement was then used for all the FE analyses to obtain a similar loading state for all damage states.

Table 2
Different damages modelled.

Size	Side	Icon	Area [mm ²]
None	None		213.8
Small	Both		189.4
Medium	Both		132.5
Large	Both		42.4
Small	Left		174.1
Medium	Left		105
Large	Left		38.5
Small	Right		174.1
Medium	Right		105
Large	Right		38.5

Experimental testing

Manufacturing

A total of 17 specimens were manufactured, with ten used for preliminary static testing and seven for the fatigue testing campaign. An automatic water-cooled diamond blade cutting machine was used to cut the adherends from large plates. The adherends were 120 mm long and 40 mm wide as shown in Fig. 2. The material properties are shown in Table 1. The adherends were joined with a circular spot weld at the centre of the overlap. To weld the adherends, the edge of the bottom adherend was clamped with a bar clamp and the top adherend was restricted using a picture frame. This frame only restricts the sideways movement, but the adherend is free to move in the direction of the sonotrode. The frame is used such that any misalignment between the adherends can be counteracted by the vertical movement which improves the quality of the welds. Instead of a conventional continuous energy director, a discontinuous energy director was used. The difference is that the continuous energy director is made of a single piece of film, while the discontinuous energy director has open areas as can be seen in the drawings in Fig. 5. The parameters of the welding process were determined through trial and error, and shown in Table 3. For more details regarding the ultrasonic welding process, the reader is

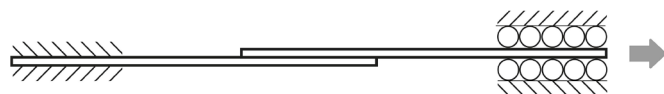


Fig. 4. Boundary conditions for the FE models.

Table 3
Welding parameters.

Parameter [Unit]	Value
Energy directory type	discontinuous
Thickness energy director [mm]	0.320
Sonotrode diameter [mm]	20
Peak-to-peak amplitude [μm]	70.8
Welding time [ms]	700
Welding force [N]	800
Consolidation time [ms]	4000
Consolidation force [N]	800

Table 4
Static failure load.

Parameter	Value
Mean failure load	10964 N
stdev of failure load	1854 N
B-basis allowable	7624 N

referred to the work of Villegas (2019). To align the loading during the fatigue tests, tabs were bonded to both ends of the specimens with cyanoacrylate and cured at room temperature. The tabs were made from the same material as the adherends. Lastly, the specimens were prepared for the DIC measurements, with the surface painted white on both sides with spray paint, followed by a black spray that created a random pattern of black speckles. Ideally, the black speckles span 3 to 5 pixels on the images, which is between 0.17 mm and 0.28 mm for the chosen set-up.

Test parameters

Before the fatigue tests were performed, a series of 10 static tests were executed on a 250 kN Zwick tensile/compression testing bench. The results for the static failure load can be seen in Table 4. The B-basis allowable was calculated and 80% of this value was used as the initial maximal cyclic load for the fatigue tests.

The fatigue tests were performed on a custom-made 60 kN fatigue test bench. To avoid unstable crack growth, the fatigue tests were performed with displacement as the control mode. The specimens were loaded to the desired maximal cyclic load that was obtained from the static tests and the displacement was registered. This displacement was used as the maximal cyclic displacement, and Table 5 shows the opening displacement for all specimens. This initial determination accounts for the test machine compliance and ensured that all specimens were loaded under more similar conditions. The fatigue test was then performed with a frequency of 5 Hz and a load ratio of 0.2. The load ratio ensured that the specimen was always loaded in tension. Thermoplastic materials are viscoelastic, therefore viscoelastic heat will be generated when they are subjected to a high-frequency loading (Villegas, 2015). This viscoelastic heat could influence the damage behaviour and should thus be avoided as much as possible. The loading frequency in these experiments was chosen to be in line with similar experimental campaigns (Leciñana et al., 2023; Sioutis and Tserpes, 2023).

Measured quantities

DIC - local surface displacement and strain measurement The local displacement on the surface of the specimens was measured using a stereoscopic DIC system with two Grasshopper 3 cameras on each side of the specimen. The data acquisition was performed with the VIC-Snap software by Correlated Solutions (2023b). The cameras had a focal length of 50 and 23 mm on the front and back of the specimen respectively. The cameras on both sides were positioned such that their field of view was similar. The speckle pattern was applied on the specimens by using a full coat of white paint with black speckles that were spray painted on top. More details regarding the DIC data acquisition and processing as well as some reference images of the speckled specimens can be found in the online dataset related to this publication (Smeets et al., 2022) A dwell of one second between each 50 fatigue cycles was implemented before and after an image was taken to ensure that there was no movement of the specimen in the images. Fig. 6 shows how the data points were integrated into the cyclic loading.

The raw data from the DIC measurements is expressed in pixel coordinates where the coordinates of the top left corner are (0px,0px) and the bottom right corner is at (2048px,2248px). The post-processing of the data with the Vic-3D 8 software (Correlated Solutions, 2023a) also used pixel coordinates. For a more straightforward interpretation, the graphs showing processed results have axes using millimetres as well as pixels.

Global displacement and reaction force The global reaction force of the specimens was measured by the fatigue testing bench with a peak-valley measurement such that every cycle was recorded. The global displacement in the specimen was measured by applying a virtual extensometer on the DIC measurement data. The virtual extensometer was obtained by extracting the relative displacement between 2 points on the surface, but does not use the complete surface of the DIC data.

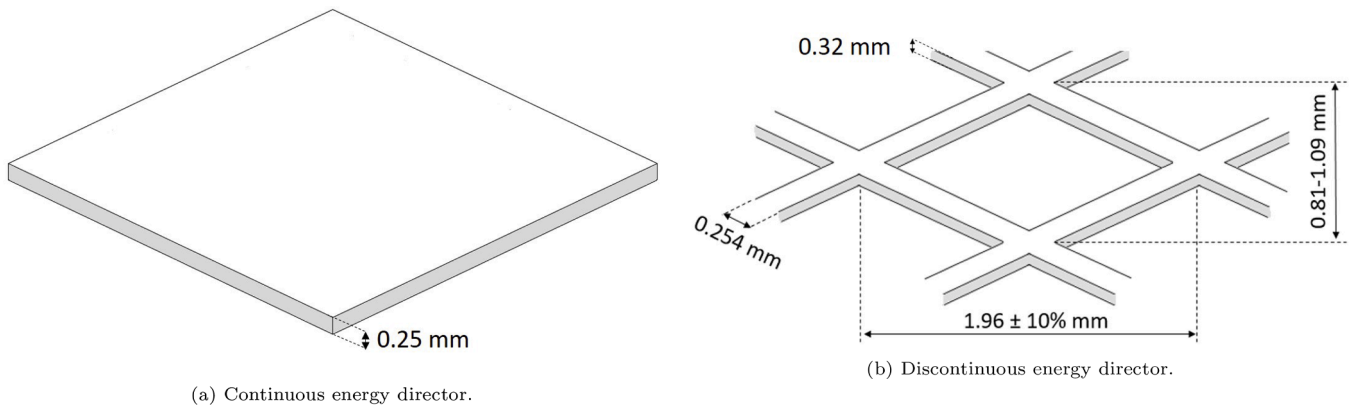


Fig. 5. Schematic representation of two types of energy directors.

Table 5
Applied opening displacement for all specimens.

Specimen	Displacement [mm]
1	0.402
2	0.383
3	0.409
4	0.353
5	0.397
6	0.403
7	0.379

Fracture surfaces

After the fatigue tests were performed, an image of the fracture surface was made with the Keyence VR-5000 3D measurement system (Keyence, 2022). These images were used to gather knowledge about the initial state of the weld area and compare it to the state that was extracted from the local surface data.

Local surface data processing

The DIC images were first processed with the Vic-3D 8 software (Correlated Solutions, 2023a) to correlate the stereo images and obtain the local displacement in all three directions. From this displacement field, a virtual extensometer can be defined to track the global compliance change of the specimen and the displacement field was converted to a strain field using a Lagrangian finite strain formulation.

In the FE analyses the local strains and displacements in all three directions were extracted at every node on the surface.

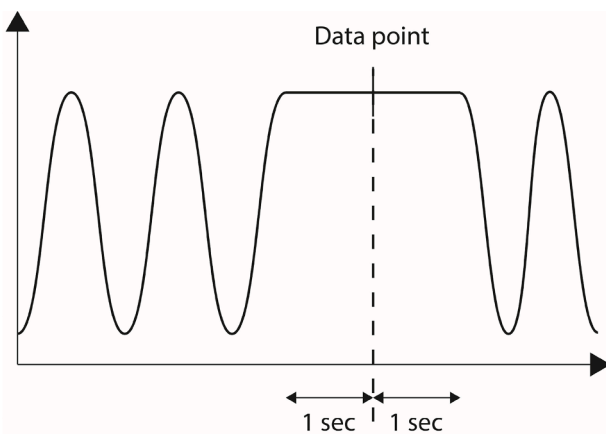


Fig. 6. DIC data points in the cyclic loading.

The output data of both the FE analyses and the experimental tests were processed with the same procedure. The strains in the two principal directions (ϵ_{xx} and ϵ_{yy}) were smoothed using the half-cosine function by Arboez (1982). The function is as follows:

$$f = \sum_{j=0}^n \sum_{i=0}^m \cos\left(\frac{i\pi x}{L}\right) (A_{ij}\cos(j\theta) + B_{ij}\sin(j\theta)) \tag{1}$$

where, A_{ij} and B_{ij} represent the amplitudes of the corresponding shape functions, and L is the width of the specimen. An added benefit of smoothing is that the discrete data is represented with continuous functions, meaning that the first and second partial derivatives can be analytically calculated using the amplitudes of the shape functions.

The amplitudes for the shape functions were computed with the “dicpp” Python module version 0.1.7 (Castro, 2021; Castro et al., 2021), which uses a linear least-squares algorithm to calculate the coefficients A_{ij} and B_{ij} . In this work, a value of $m = n = 6$ was assumed, providing enough detail to allow the other processing steps, while still filtering out enough noise from the data by omitting the higher-order frequency terms from the half-cosine function. After the calculation of the shape functions, a five-step process was followed:

1. Choose 5 vertical probing lines along the surface of the overlap (Fig. 7a and b). The data was transformed such that both sides of the specimen use the same coordinate system. The coordinate system of both sides is determined using the four corners of the overlap. With this information, the coordinate transformation between the back and the front side could be determined and all the data could be represented in the same system. The choice to use 5 probing lines was made to provide enough detailed information while not using too much computational power during the processing of the data.
2. Extract the data along the probing lines (Fig. 7c).
3. Find local minima and maxima on the 5 probing lines on both sides of the specimen using the partial derivative $\partial f / \partial y$ (Fig. 7c). In a SLS specimen, the tension on the specimen causes secondary bending due to misalignment of the adherends. In the locations where the adherends are still attached, the neutral axis of the secondary bending changes, causing a local minimum or maximum in the strain in the vertical direction. Thus, by locating the local minima and maxima, possible weld locations can be detected. The displacement and strain data from both sides were combined to get a complete view of the damage state. On the front side, the data from the top half of the overlap was used and on the back side, the data from the bottom half was used. The adherend on the front is loaded from the top, thus the bottom half of the overlap is unloaded and this means that the peaks in the strain often don't surpass the noise in the signal. Therefore only the data from the top half of the front was used. Since the specimen is anti-symmetric, the same reasoning applies to the

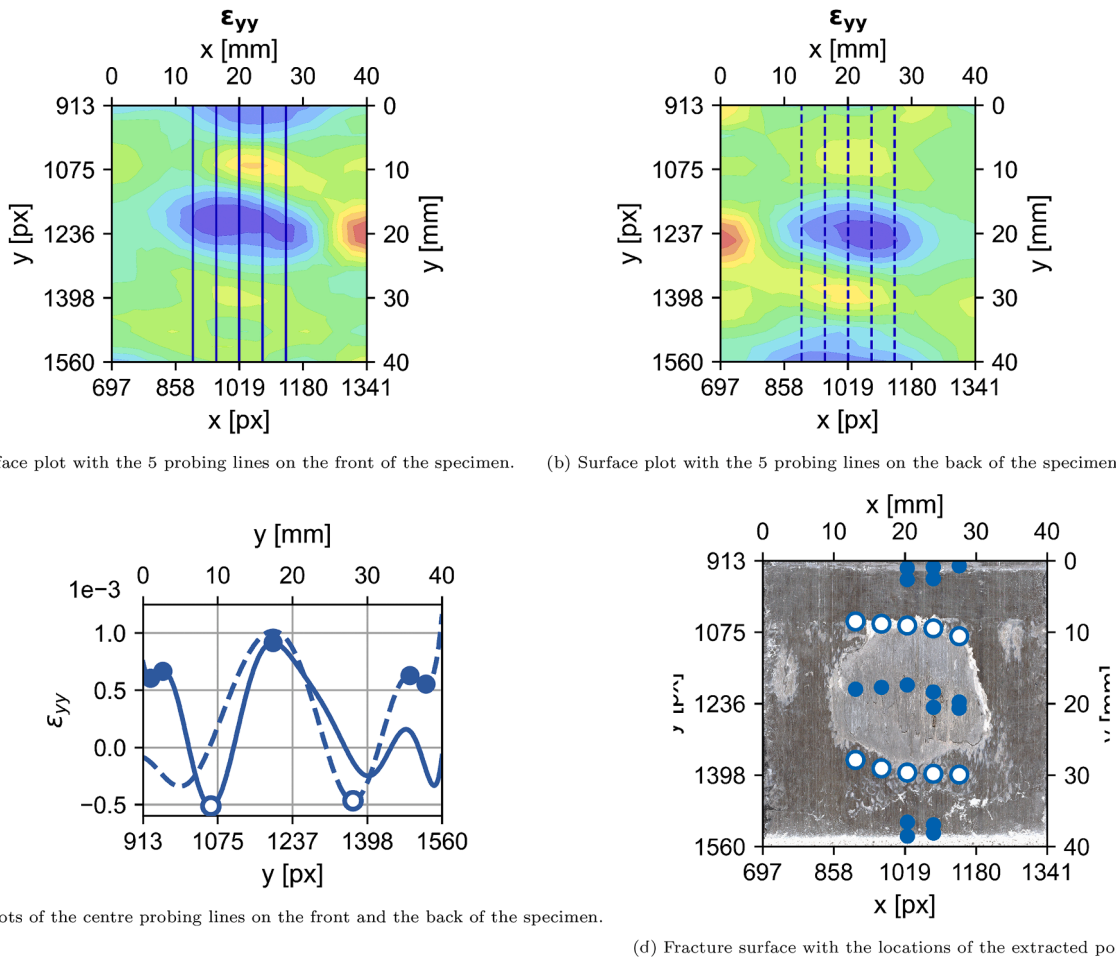


Fig. 7. Processing the surface strain data. Points on the weld edge are indicated with open dots and false positives with closed dots.

bottom half of the back. This does assume that the centre of the spot coincides with the centre of the overlap, but since the specimens were manufactured by welding the centre of the overlap, this assumption is not expected to impact the results.

- Fig. 7d shows that the false positives were located outside of the weld boundary and at the centerline of the weld. These false positives were removed from the calculations by first identifying which points were located within the initial boundary of the weld and afterwards removing the points that were not the outer two points on each probing line, thus removing the false positives around the centerline.
- Determine weld area by calculating the distance between the points on each line to calculate the area for that section and summing the areas of the 5 probing lines as shown in Fig. 8. The damage was represented as a percentage of the initial weld area.

The results from the FE analyses were processed first. The processed FE results served as a verification tool for the processing steps. The choice of the number of probing lines, the use of local minima and maxima, and the locations of the false positives were determined during the FE post-processing. Once all these aspects were verified, the processing procedure was applied to the experimental data in the same way. Furthermore, the FE results also showed that the quantities of interest are the in-plane strain in the vertical direction and the second derivative of the out-of-plane displacement since the latter is inversely related to the radius of curvature (Megson, 2013). It was not necessary to simulate the complete fatigue life of the specimens in the FE analyses since the variety of damage states made sure that the processing steps could be verified during the whole fatigue life of a representative specimen.

For the FE results, this procedure was only applied once, whereas, for

the experimental data, the procedure was applied for every data point to obtain a damage growth curve for the complete fatigue life.

Results

Fracture surfaces

Fig. 9 shows the fracture surface of two different specimens after the fatigue test was completed. Two different specimens were chosen. Specimen 1 is a regular shape that is close to the ideal circular weld, while specimen 2 has a much more irregular shape. To easily distinguish the two, specimen 1 will be denoted with a ● symbol and specimen 2 with a ⬤ symbol.

Global reaction force and displacement

Numerical analyses

In the numerical analyses, the area of the weld was known beforehand. Fig. 10 shows the global compliance and the weld area from these analyses for the different damage types that were modelled. The compliance was determined at the same global displacement for each analysis.

Experimental tests

The displacement obtained with the DIC measurements was used to calculate the global displacement during the fatigue life. The resulting global compliance during the test is shown in Fig. 11a. The difference in fatigue life between both specimens seems rather large. However, this is

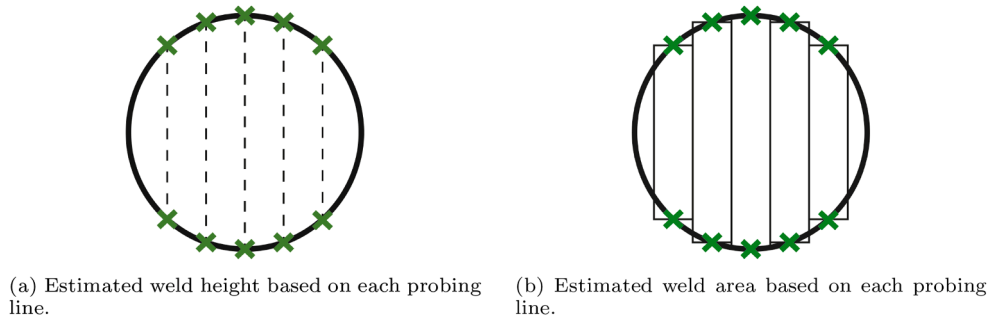


Fig. 8. Weld area estimation based on extracted weld edges.

a common variation in fatigue damage growth. Due to the complex and stochastic nature of fatigue loading, there is often a large variation in the fatigue life of different specimens with the same configuration. Especially considering the difference in size and shape between the 2 specimens. Furthermore, Fig. 11b shows that the damage behaviour of both specimens is very similar, with specimen 2 simply showing a larger damage propagation phase, which can be seen from the longer plateau in the compliance.

Out-of-plane displacement

Numerical analyses

The second derivative of the out-of-plane displacement was calculated and shown in Fig. 12 for the FE analysis without pre-existing damage. The data was extracted along the probing line at the centre of the specimen.

Experimental tests

The second derivative of the out-of-plane displacement was calculated using the coefficients from the Fourier fitting and shown in Fig. 13. The data was plotted along the probing line at the centre of the specimen.

Surface strain

Numerical analyses

The processing steps described in the Methodology were applied to the numerical data and the experimental data. Fig. 14 shows the known weld edges and extracted weld points for the numerical analysis of the undamaged weld.

The processing was applied to all the numerical analyses to compute the welded area for each one. The result can be seen in Fig. 15 where the measured weld areas are compared to the known weld areas.

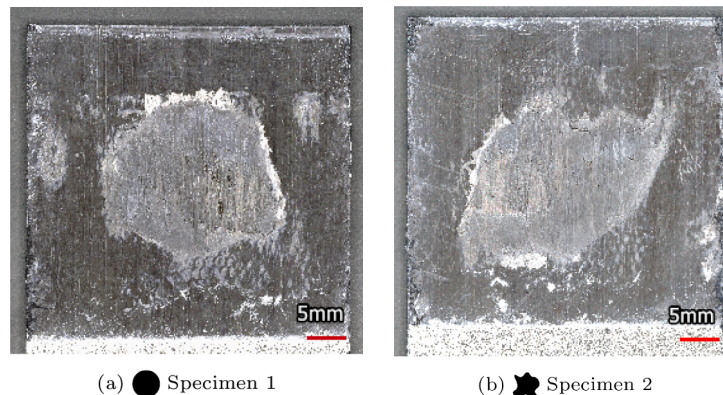


Fig. 9. The fracture surface of two of the specimens after the completion of the test, taken with the Keyence microscope (Keyence, 2022).

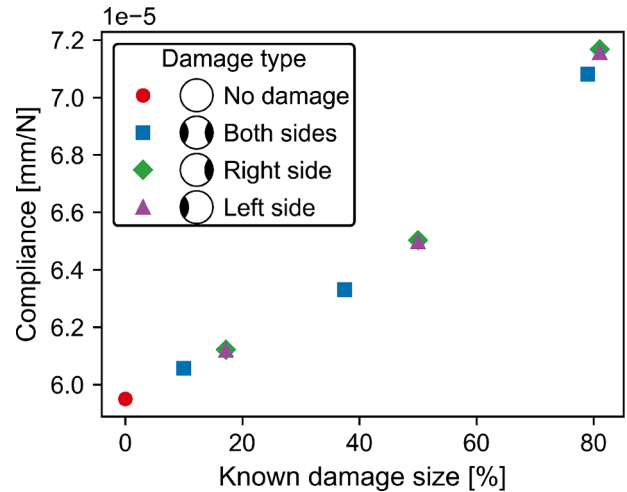


Fig. 10. Known weld area and global compliance from the numerical analyses.

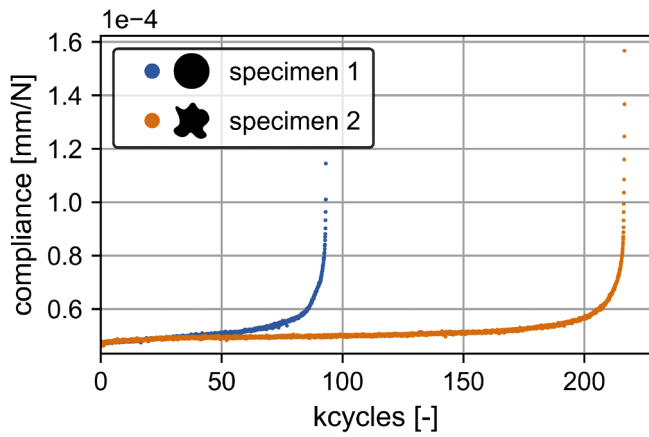
Experimental tests

Applying the same procedure to the strains that were measured by the DIC results in the images in Fig. 16. The results for two different specimens are shown on top of an image of their fracture surface at four different moments during the fatigue life of the specimens.

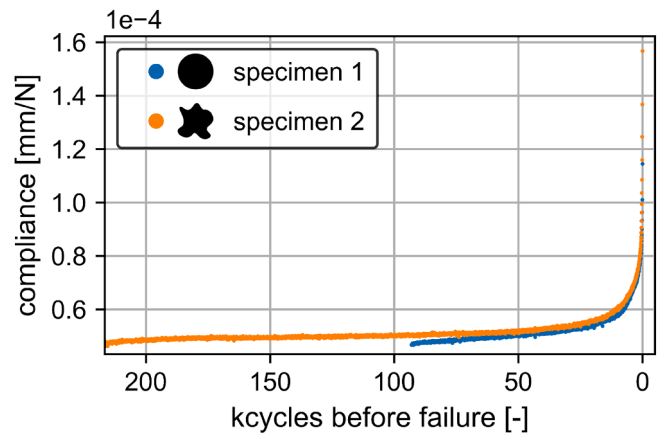
To observe the damage evolution behaviour of the specimens, processing steps were applied for each DIC data point during the fatigue life of the specimens. This is shown in Fig. 17.

Discussion

The goal of this study was to compare different measurement techniques in the context of providing a reliable measurement of the damage



(a) Comparison of applied fatigue cycles



(b) Comparison of cycles until final failure

Fig. 11. Global specimen compliance during the fatigue life for the two different specimens shown in Fig. 9.

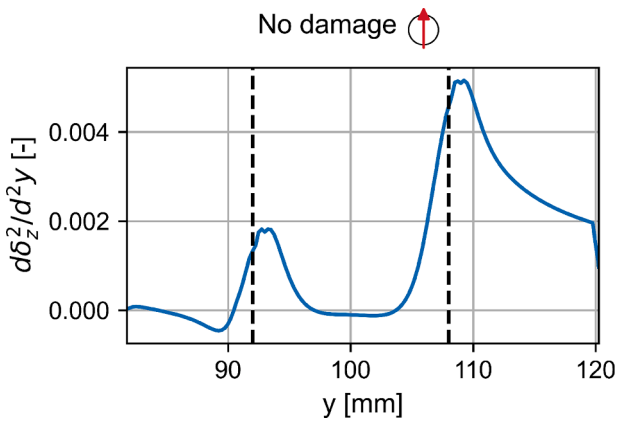


Fig. 12. Second derivative of the out-of-plane displacement along the centre of the specimen for the FE analysis without pre-existing damage. The dotted vertical lines indicate the known locations of the weld edge.

growth in single ultrasonic welded joints with the perspective of expanding the configurations to multiple spot welds. The three measurements were the global compliance, the local out-of-plane

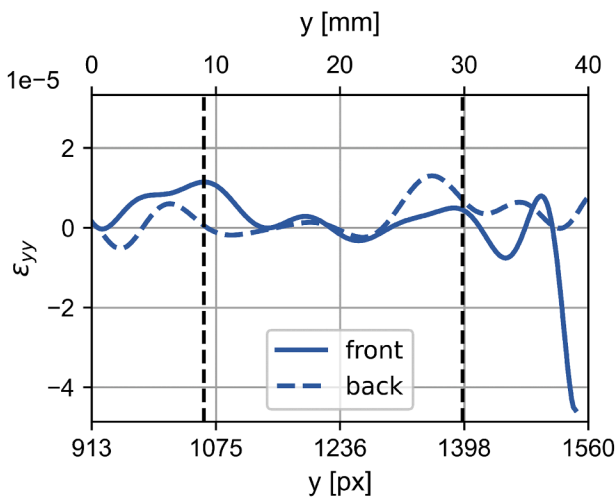
deformation and the local surface strain.

Global compliance

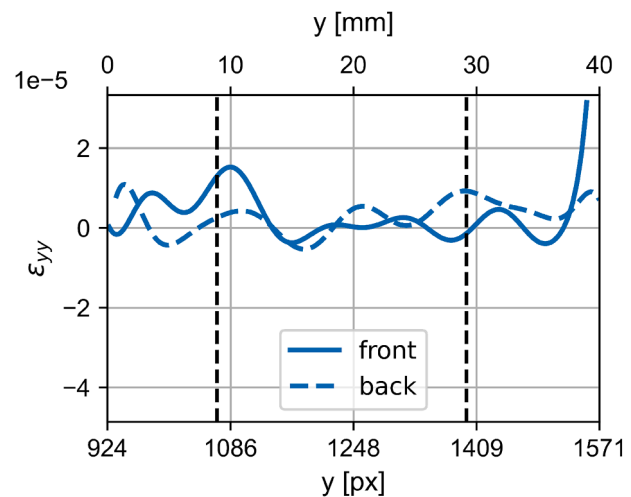
Based on the FE results presented in Fig. 10, it can be concluded that the global compliance correlates very well with the total amount of damage in the welded joint. However, since this measurement only uses data concerning the global state of the specimen, the information that was obtained from it was also global. The FE analyses where damage was modelled on both sides, exhibit the same relation as those where damage was only modelled from one side. This shows that detailed information such as the location of damage growth cannot be obtained with this method.

Out-of-plane deformation

In SLS specimens, the loading and the neutral axis of the specimen are not aligned, resulting in an out-of-plane deformation of the specimen due to secondary bending. Because the neutral axis changes when there is an intact weld present at the interface, it was expected that the radius of curvature of the secondary bending changes at the border of this intact weld. The radius of curvature of the bending is approximately equal to the inverse of the second derivative of the displacement



(a) Specimen 1



(b) Specimen 2

Fig. 13. Second derivative of the out-of-plane displacement along the centre of the specimen for two of the specimens at the start of the fatigue life. The dotted vertical lines represent the estimated locations of the weld edge.

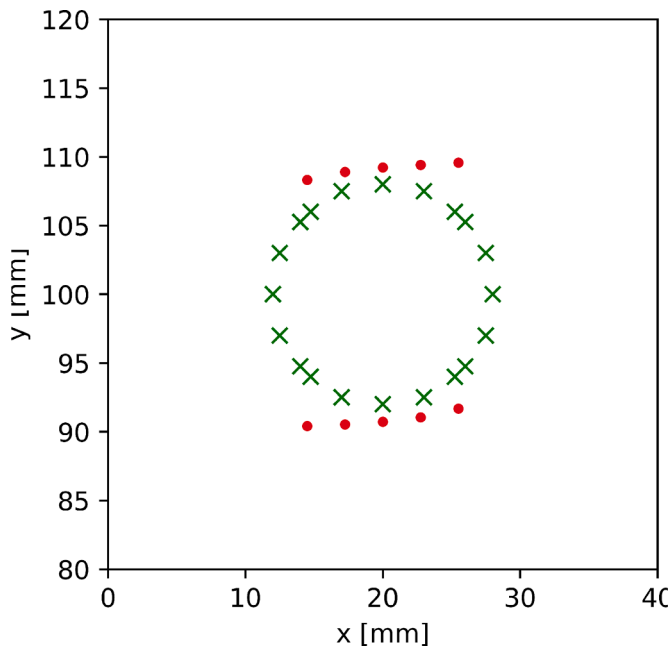


Fig. 14. Weld edges extracted from the surface strain of the numerical analysis without pre-existing damage. The crosses are the known locations of the weld edge, the red dots are the extracted locations.

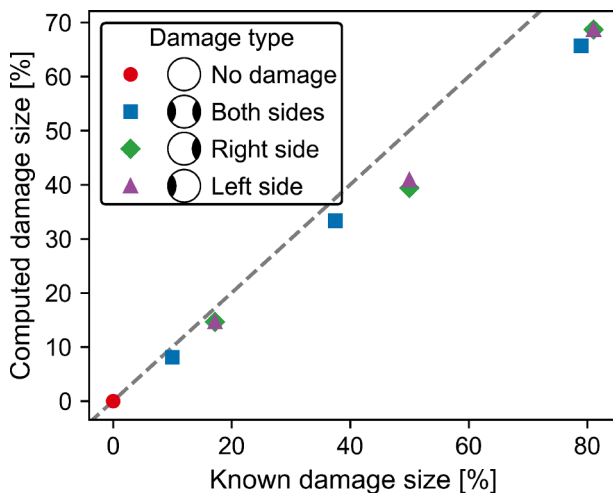


Fig. 15. Measured and known weld areas of the numerical analyses. The dotted grey line represents the ideal scenario where the computed and known damage sizes would be equal.

(Megson, 2013). In the FE results in Fig. 12 it can be seen that peaks in the second derivative of the out-of-plane displacement indeed align with the edges of the damage quite well.

However, the equivalent results from the DIC measurement in Fig. 13 show that this reasoning cannot be applied here. The DIC data inherently has some noise. The changes in the second derivative that should be seen at the edges of the damage, were so small that it was not possible to distinguish them from the noise in the signal. This means that the filtering steps that were applied to the data cannot separate the noise from the signal, therefore the peaks cannot be detected in the out-of-plane displacement of the DIC measurements.

Surface strain

Numerical analyses

Some of the locations of local maxima and minima of the strain coincide with the known edges of the welds at the interface. Fig. 14 shows that after removing the false positives at the centre of the weld and outside of the weld area, the extracted points show a good correlation to the known boundary of the weld. Although we can already visually observe which points were false positives, the filtering step in the procedure in the Methodology was necessary to be able to obtain a single quantity for the remaining weld area from the cloud of points. It should be noted that to apply this filtering, the initial location of the boundary of the weld has to be known beforehand. After performing the same computations for all the modelled damages, Fig. 15 shows that the evolution in the computed damage size matches the evolution in known damage size. Although there was a quantitative difference between the computed and known damage sizes, the plot shows a linear relationship between the two, therefore it can be concluded that the qualitative evolution of the damage was extracted quite well.

Experimental tests

Fig. 16 shows the extracted points on the fracture surface for different points of the fatigue life. This figure is the result of the processing steps in the Methodology. Some considerations regarding the filtering of the points and its effect on the final results should be made:

- The false positives appear either outside of the initial weld region or in the centerline of the weld during the first 80 to 90 % of the fatigue life. Therefore step four, the filtering step can be applied without interfering with the data.
- The extraction of the points at the start of the fatigue life can be validated with certainty because at this point in time it can be assumed that the boundaries of the weld were the same as what can be seen on the fracture surface afterwards.
- Towards the very end of the fatigue life, the extraction of points tends to 'explode', meaning that the extracted points grow outward with respect to the ones from previous timestamps. What happens, in this case, is that the damage has grown so much that the strains as a result of the secondary bending obscure the local minima and maxima corresponding to the weld edge. Since the fourth processing step in the Methodology was forced to choose two points on each probing line, the chosen points were further apart. Since this only happens in the last 10 to 20 % of the fatigue life, this part of the data can simply be disregarded without losing information on the damage evolution.
- Similar to the previous point, when the damage has grown beyond the location of a probing line, i.e. the weld does not cross that line anymore, the fourth processing step still chooses two points on that line, meaning that this data was also nonsensical. Since the damage in SLS specimens mostly grows in the y direction, this does not pose a problem until the very end of the analysis.

The overall damage data in Fig. 17 shows significant noise. This is because a DIC image was taken every 50 cycles, which means that the data was oversampled. To overcome this, an extra filtering step can be applied. There are two readily available options to filter the data, the half-cosine Fourier fitting that was used to apply an initial filter as explained in the Methodology and the incremental polynomial technique outlined in ASTM E647 (ASTM Standard E647, 2016) are both suitable techniques. The method from ASTM is a well-known method to smooth crack growth data and obtain the crack growth rate at the same time. The disadvantage is that a number of points (equal to half of the subset size) are lost at the start and end of the analysis. This can be somewhat overcome by decreasing the subset size near the edges of the data set. The half-cosine Fourier approximation does fit the whole data set, however, the approximation will always go towards zero at the edges. An added disadvantage is that plateaus in the data are much

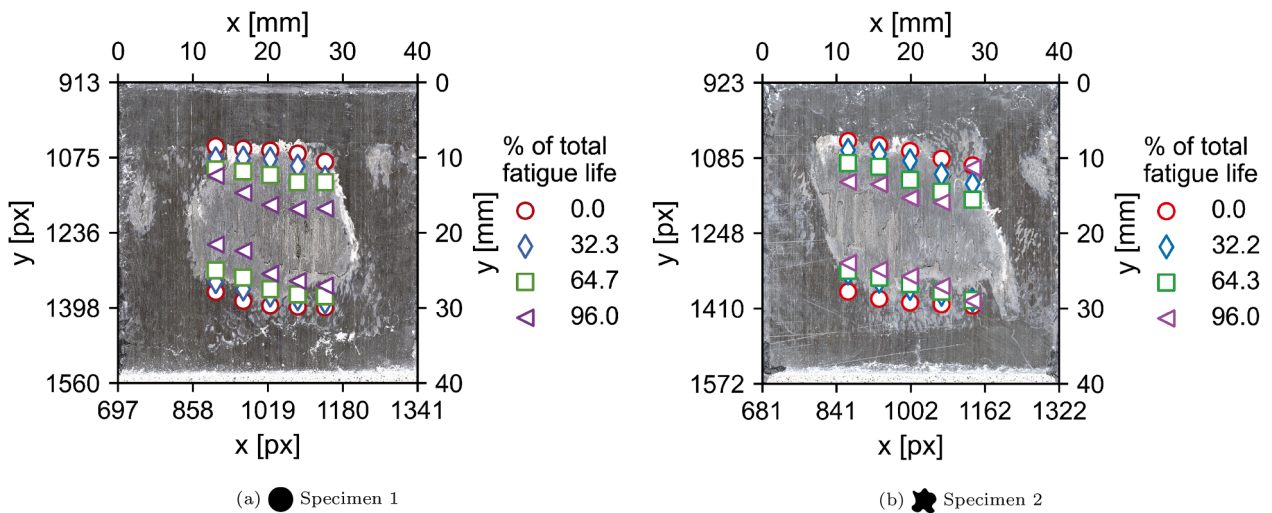


Fig. 16. Weld edges extracted from the surface strain of two of the specimens overlaid on an image of the fracture surface.

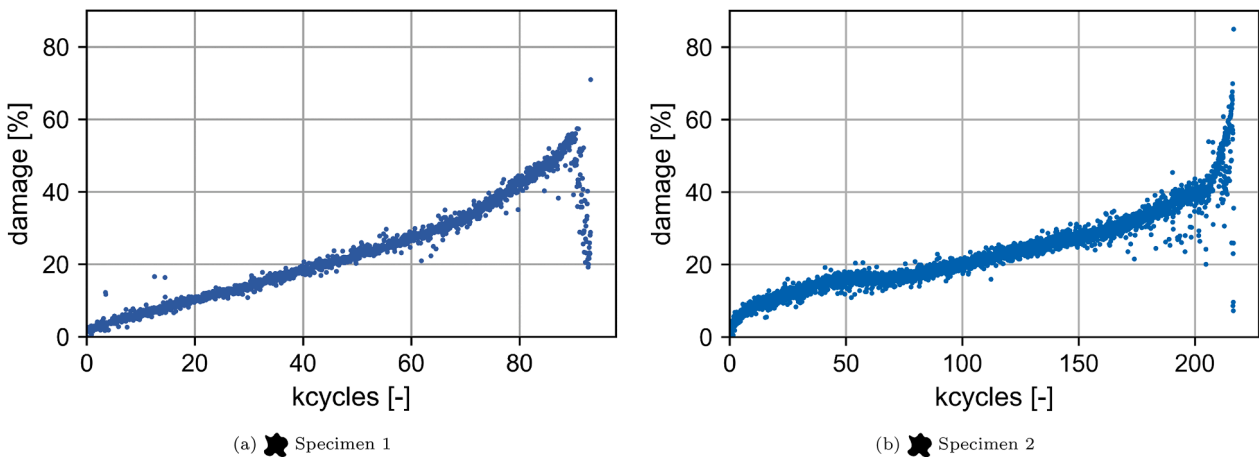


Fig. 17. Extracted weld area during the fatigue life of the two specimens shown in Fig. 9.

harder to approximate with the Fourier method. This is especially relevant with the expansion to multi-spot welded joints in mind since a damage arresting behaviour could be expected in these joints. Therefore, the ASTM method with a minimum of 101 data points and a maximum of 601 data points was used here, these values resulted in enough smoothing to overcome the sampling without losing data. The result is shown in Fig. 18. The ASTM method also allows for the calculation of the first derivative, which is shown in Fig. 19

Since the global compliance does give a good global view of the damage in the joint, the data obtained through the surface strain can be compared to it in order to verify the measurements. The compliance data was smoothed in the same way as the damage measurements.

The comparison in Fig. 19 shows that there was a good correlation between both results. This shows that the surface strain does result in a good representation of the damage growth behaviour. However, some differences can also be seen in this comparison. These deviations were probably a result of damage growth in the direction transverse to the loading. The surface strain method only captures the growth along the loading axis. The strains along the transverse direction were the result of the Poisson contraction of the adherends, therefore the peaks in the strain were much lower. Extracting the edges of the damage along this axis would run into the same issue as with the out-of-plane displacement in the sense that it would not be feasible to distinguish the actual peaks from the noise in the data.

These results show that the exact damage state of the spot welds can

be extracted from the local strain on the outer surfaces of the SLS specimens. However, external intervention is always necessary for some of the processing steps. Especially the filtering of the false positives requires the definition of the initial bounding box of the spot weld to be inserted in the processing code. In the current application of a single spot at the interface, this is feasible, but this might impact the extension to larger configurations.

The specimen specifications, such as the materials used, the type of energy director, and the lay-up of the adherends, will have an effect on the damage growth through the spot welds. The focus of this work was to provide a method of capturing the damage growth. The parameters that affect the damage growth were not studied. The methods presented in this paper can be used in future work to study these effects.

Multi-spot welded joints

The purpose of this research was to study the different measurement techniques in the context of characterizing the damage progression in multi-spot welded joints. As a first step, the techniques were applied to single-spot joints and the results were evaluated in the previous sections. The expansion of these analyses to multi-spot welded joints and possible challenges should also be discussed.

In the case of a multi-spot arrangement, the shortcoming of compliance as a measure of the damage growth is even more impactful. An important aspect when characterizing the damage progression is the

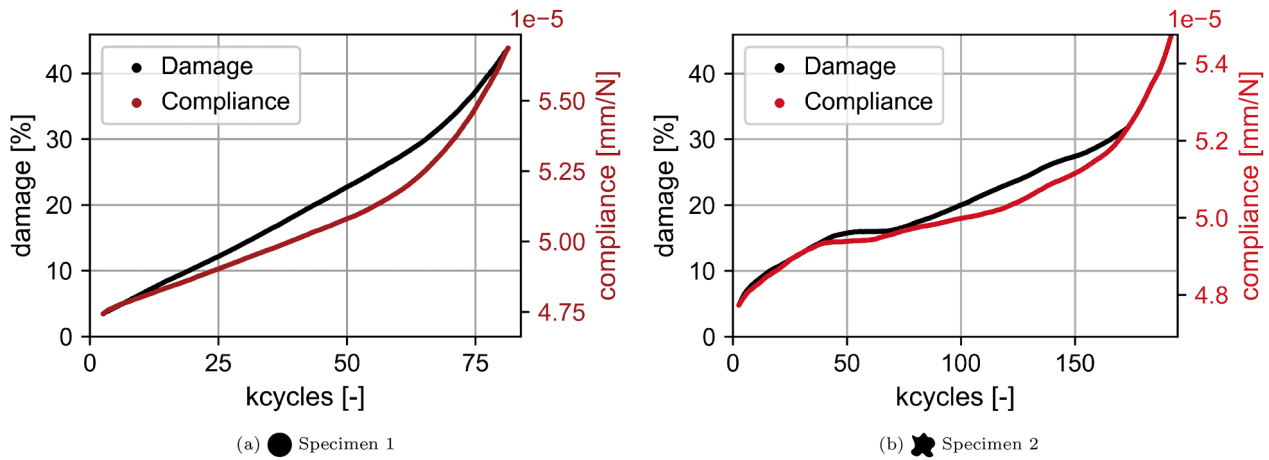


Fig. 18. Smoothed damage percentage and compliance during the fatigue life of the two specimens shown in Fig. 9.

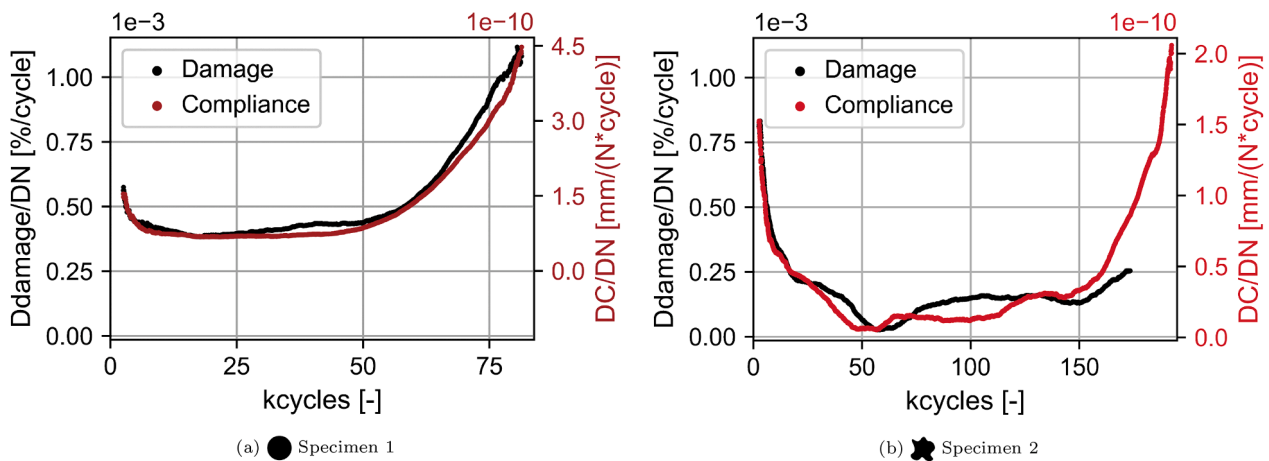


Fig. 19. Smoothed damage growth rate and compliance change during the fatigue life of the two specimens shown in Fig. 9.

sequence of damage initiation and complete failure of the different spots. Due to the global nature of the compliance, it is not possible to obtain this information with only this measurement technique. However, in the analysis of these specimens, the measurement of the compliance can still serve as a verification method.

In the processing of the surface strain results, it was observed that the strain peaks at the unloaded side of the specimen do not always surpass the noise in the data. To overcome this, the measurements from both sides were used and the information was combined. However, in a multi-spot arrangement, this solution might not be as simple. Consider, for example, a configuration with four spots aligned in the loading direction. In such a configuration, only the outer edges of each outer spot are highly loaded. Furthermore, the area of interest will be larger, which means that the spatial accuracy of the DIC measurements is reduced. The result of these two factors is that the strain peaks at the inner edges of the spot welds will likely not surpass the noise in the DIC measurements on either side of the specimen, making it impossible to extract the locations of these edges. Since these edges are not as highly loaded, it can be assumed that the damage growth here will be significantly slower than at the loaded edges, but it cannot be assumed that the damage growth is non-existent without proof.

Another aspect that makes the analysis of multi-spot joints more challenging is the combination of strain measurements from both sides. In the single spot joints, this combination was made based on the assumption that the centre of the intact weld coincides with the centre of the overlap and that the damage does not grow beyond the centre of overlap from either side. In the case of a multi-spot welded joint, not all

spots will be located at the centre of the overlap and damage could grow beyond the centre of the overlap, depending on the configuration. This could be solved by using a separate 'bounding box' for each of the spots and combining the information for each bounding box separately. This will require careful analysis to ensure that the data from the front and the back sides are transformed correctly.

With the current method to process the strain data, two points are always chosen per probing line for every time step. However, when a spot is fully damaged, these two points would also still be identified. Therefore, the strain data on its own is not a sufficient indicator to determine whether a single spot in a multi-spot arrangement is fully damaged or not. In the analysis of damage progression through a multi-spot welded joint, this is important to determine. To do this, one could either set a maximum damage percentage above which the spot is considered fully damaged. Another strategy could be to use a different measurement technique to determine this. For example, a sudden change in global compliance could also indicate that one of the spots has completely failed.

All these aspects impact the feasibility of the expansion of the method to larger configurations. The challenges can be overcome when considering arrangements with four spots on lab-scale specimens, but their effect will be significantly increased with a larger amount of spots. Furthermore, the method relies on the DIC measurements, which require the specimens to be painted and speckled. Applying this outside of a lab context is very time-consuming. This means that while the method is suited to be applied in a lab environment, the application outside of that environment will not be as straightforward.

Conclusion

To find a method to confidently determine the damage growth behaviour in single ultrasonic spot welded joints, three measurement techniques were compared. FE analyses were used to investigate how damage growth influences these techniques and to observe the phenomena that would have to be found in the experimental data to characterize the damage growth.

Firstly, the global compliance of the specimen was determined. Only information about the global damage state of the system can be obtained. Since the measurement does not use any local quantities, a detailed view of the damage state cannot be obtained.

The second quantity investigated was the out-of-plane displacement over the whole surface, measured with DIC imaging. The FE results showed the peaks in the second derivative correspond to the weld edges, due to a change in the neutral axis of the secondary bending in the spot location. However, it was found that the noise in the experimental data was so large that the peaks were not distinguishable.

The last quantity of interest was the in-plane strain over the whole surface. This quantity was also obtained from the DIC images. The FE results showed that the locations where the first derivative of the vertical strain is equal to zero coincided with the known locations of the edge of the undamaged welds. When applying the same method to the experimental data a good correlation between the damage growth and the compliance was seen, as well as a good correlation between the change in damage and the change in compliance per cycle. This confirms that the surface strain is a quantity that can be used to determine the growth of damage.

Based on these results, it can be concluded that the surface strain provides the most detailed information on the damage growth in single ultrasonic spot welded joints. However, it should be noted that this measurement does not show the full story either, for example only the damage growth in the direction of the loading is measured. In some cases, it could be useful to also include the global compliance to get a better view of the complete damage growth behaviour of the specimens. Furthermore, the DIC measurement technique requires the surface to be speckled to produce images of a high enough resolution with a reference image such that they can be correlated to each other. In a lab environment, this requirement is easily fulfilled, but in a service environment or on full-scale aircraft this will be more complex. The damage observation technique proposed in this paper is thus better suited to gain an understanding of the damage behaviour of ultrasonic spot welded joints on a coupon level rather than an in-service structural health monitoring technique.

Declaration of Competing Interest

The authors declare that they have no known competing financial interests or personal relationships that could have appeared to influence the work reported in this paper.

Data availability

The data related to this paper is accessible through the 4TU Research Data repository at <https://doi.org/10.4121/21667796>.

References

Arbocz, J., 1982. The Imperfection Data Bank, a Mean to Obtain Realistic Buckling Loads. Springer Berlin Heidelberg. https://doi.org/10.1007/978-3-642-49334-8_19.

- ASTM Standard D5868-01, 2005. Standard Test Method for Lap Shear Adhesion for Fiber Reinforced Plastic (FRP). ASTM International, West Conshohocken, PA. <https://doi.org/10.1520/D5868-01R14.2>.
- ASTM Standard E647, 2016. Standard Test Method for Measurement of Fatigue Crack Growth Rates. ASTM International, West Conshohocken, PA. <https://doi.org/10.1520/E0647-00>.
- Carboni, M., Bernasconi, A., 2021. Acoustic emission based monitoring of fatigue damage in CFRP-CFRP adhesive bonded joints. European Workshop on Structural Health Monitoring, Vol. 127, pp. 605–615. https://doi.org/10.1007/978-3-030-64594-6_59.
- Castro, S. G., 2021. Digital image correlation post processing module version 0.1.7. Accessed: 16-05-2023, <https://pyipi.org/project/dicpp/0.1.7/>.
- Castro, S.G., Almeida Jr, J.H.S., St-Pierre, L., Wang, Z., 2021. Measuring geometric imperfections of variable-angle filament-wound cylinders with a simple digital image correlation setup. Compos. Struct. 276, 114497. <https://doi.org/10.1016/j.compstruct.2021.114497>.
- Correlated Solutions, 2023a. VIC-3D 8. Accessed: 16-05-2023, <https://correlatedsolutions.eu/software/vic-software>.
- Correlated Solutions, 2023b. VIC-Snap. Accessed: 16-05-2023, <https://www.correlatedsolutions.com/vicsnap>.
- Federal Aviation Administration, 2009. AC 20-107B: composite aircraft structure.
- Holzhueter, D., Löbel, T., Hühne, C., 2018. The adhesive zone mix disbond arrest feature results (EU-FP7 project BOPACS). AVT-266 Research Specialists' Meeting on Use of Bonded Joints in Military Applications.
- Jairaja, R., Naik, G., 2021. Weak bond effects in adhesively bonded joints between the dissimilar adherends. J. Adhes. 97 (8), 760–782. <https://doi.org/10.1080/00218464.2019.1702027>.
- Karimian, S.F., Modarres, M., 2021. Acoustic emission signal clustering in CFRP laminates using a new feature set based on waveform analysis and information entropy analysis. Compos. Struct. 268, 113987. <https://doi.org/10.1016/j.compstruct.2021.113987>.
- Keyence, 2022. VR-5000 Wide-Area 3D Measurement System. Accessed: 16-05-2023, <https://www.keyence.eu/products/microscope/macroscope/vr-3000/models/vr-5000/>.
- Leciñana, I., Renart, J., Turon, A., Zurbitu, J., Tijs, B., 2023. Characterization and analysis of the mode I interlaminar fatigue behaviour of thermoplastic composites considering R-curve effects. Eng. Fract. Mech. 109273. <https://doi.org/10.1016/j.engfracmech.2023.109273>.
- Lima, R.A., Migliavacca, F., Martulli, L.M., Carboni, M., Bernasconi, A., 2022. Distributed fibre optic monitoring of mode I fatigue crack propagation in adhesive bonded joints and comparison with digital image correlation. Theor. Appl. Fract. Mech. 121, 103501. <https://doi.org/10.1016/j.tafmec.2022.103501>.
- Megson, T.H.G., 2013. Bending of Open and Closed, Thin-Walled Beams, 5th ed. Elsevier Butterworth-Heinemann.
- Motta, R.F., Alderliesten, R., Shiino, M.Y., Cioffi, M.O.H., Voorwald, H.J.C., 2020. Scrutinizing interlaminar fatigue loading cycle in composites using acoustic emission technique: stress ratio influence on damage formation. Compos. Part A Appl. Sci. Manuf. 138, 106065. <https://doi.org/10.1016/j.compositesa.2020.106065>.
- Rodi, R., Alderliesten, R., Benedictus, R., 2009. An experimental approach to investigate detailed failure mechanisms in fibre metal laminates. ICAF 2009, Bridging the Gap Between Theory and Operational Practice - Proceedings of the 25th Symposium of the International Committee on Aeronautical Fatigue, pp. 493–512. https://doi.org/10.1007/978-90-481-2746-7_28/COVER.
- Sioutis, I., Tserpes, K., 2023. A mixed-mode fatigue crack growth model for consolidated thermoplastic joints. Int. J. Fatigue 173, 107682. <https://doi.org/10.1016/j.ijfatigue.2023.107682>.
- SKF evolution, 2022. SKF Black Design. Accessed: 16-05-2023, <https://evolution.skf.com/skf-black-design/>.
- Smeets, E., Rans, C. D., Castro, S. G. P., Villegas, I. F., 2022. Data underlying the publication: measuring fatigue damage growth of spot welded thermoplastic composites using digital image correlation 10.4121/21667796.V1.
- Smith, M., 2020. Abaqus/CAE User's Guide 2020. Dassault Systèmes Simulia Corp, Providence, RI.
- Toray Advanced Composites, 2019. Toray Cetex ® TC1225 product data sheet.
- Villegas, I.F., 2015. In situ monitoring of ultrasonic welding of thermoplastic composites through power and displacement data. J. Thermoplast. Compos. Mater. 28 (1), 66–85. <https://doi.org/10.1177/0892705712475015>.
- Villegas, I.F., 2019. Ultrasonic welding of thermoplastic composites. Front. Mater. 6, 291. <https://doi.org/10.3389/fmats.2019.00291>.
- Villegas, I.F., Bersee, H.E.N., 2010. Ultrasonic welding of advanced thermoplastic composites: an investigation on energy-directing surfaces. Adv. Polym. Technol. 29 (2), 112–121. <https://doi.org/10.1002/adv.20178>.
- Villegas, I.F., Rans, C., 2021. The dangers of single-lap shear testing in understanding polymer composite welded joints. Philos. Trans. R. Soc. A Math. Phys. Eng. Sci. 379, 20200296. <https://doi.org/10.1098/rsta.2020.0296>.
- Yousefpour, A., Hojjati, M., Immarigeon, J.P., 2004. Fusion bonding/welding of thermoplastic composites. J. Thermoplast. Compos. Mater. 17 (4), 303–341. <https://doi.org/10.1177/0892705704045187>.
- Zhou, B., Thouless, M., Ward, S., 2006. Predicting the failure of ultrasonic spot welds by pull-out from sheet metal. Int. J. Solids Struct. 43 (25-26), 7482–7500. <https://doi.org/10.1016/j.jlstr.2006.03.009>.